Chinese Journal of Aeronautics, (2014),27(6): 1461–1468

Chinese Society of Aeronautics and Astronautics
& Beihang University

Chinese Journal of Aeronautics

cja@buaa.edu.cn
www.sciencedirect.com

Design and experiments of an active isolator for satellite micro-vibration

Li Weipeng [a], Huang Hai [a,*], Zhou Xubin [b], Zheng Xintao [a], Bai Yang [a]

[a] School of Astronautics, Beihang University, Beijing 100191, China
[b] Shanghai Institute of Satellite Engineering, Shanghai 200240, China

Received 26 September 2013; revised 13 November 2013; accepted 4 December 2013
Available online 20 October 2014

KEYWORDS

Isolator;
Micro-vibration;
Satellite;
Spacecraft;
Vibration control

Abstract In this paper, a soft active isolator (SAI) derived from a voice coil motor is studied to determine its abilities as a micro-vibration isolation device for sensitive satellite payloads. Firstly, the two most important parts of the SAI, the mechanical unit and the low-noise driver, are designed and manufactured. Then, a rigid-flexible coupling dynamic model of the SAI is built, and a dynamic analysis is conducted. Furthermore, a controller with a sky-hook damper is designed. Finally, results from the performance tests of the mechanical/electronic parts and the isolation experiments are presented. The SAI attenuations are found to be more than −20 dB above 5 Hz, and the control effect is stable.

1. Introduction

For most satellites, on-board devices with moving/rotating mass, such as momentum or reaction wheels, flexible manipulator systems, cryocoolers, and other specialised devices, create micro-vibrations.[1–4] In the past, micro-vibrations with low amplitudes and frequencies up to approximately 1 kHz have often been neglected because of the low levels of induced disturbances.

Today, many satellites require very quiet environments to protect sensitive payloads, such as laser communication devices, astronomical telescopes, and micro-gravity experimental instruments. In order to achieve these stringent requirements, research on the attenuation of satellite micro-vibrations has become much more important. A variety of satellite designs and control architectures have been studied.[5,6] The most important aspect of satellite design and control is the vibration isolation between the precision payload and the disturbance base, which provides perfect transmissibility at low frequencies, greater isolation at high frequencies, and minimal amplification at all frequencies.

Commonly, passive isolation is regarded as the most mature technology for managing in-orbit vibration isolation. Ref.[7] discussed a two-layer vibration isolator assembly on the James Webb space telescope, which used viscoelastic damping with titanium springs and graphite/epoxy beams. Ref.[8] created a compact isolator for a space imager that was composed of three C-shaped metal springs with rubber dampers. Ref.[9] studied a viscoelastic damped ball joint and demonstrated its space applications, such as reaction wheel isolator struts. Ref.[10]

* Corresponding author. Tel.: +86 10 82316611.
E-mail addresses: liweipeng@buaa.edu.cn (W. Li), hhuang@buaa.edu.cn (H. Huang).

Peer review under responsibility of Editorial Committee of CJA.

ELSEVIER Production and hosting by Elsevier

http://dx.doi.org/10.1016/j.cja.2014.10.012

developed a three-parameter isolator (D-strut) for a reaction wheel, in which the damping force was produced by a viscous fluid. Ref.[11] proposed a simple isolator, which consisted of a spring in parallel with an electromagnetic Maxwell unit. Passive isolation is necessary to limit the amplification at resonance but tends to reduce high-frequency attenuation. Furthermore, the damping materials are unable to maintain their properties in the harsh space environment because of their temperature dependence, making them insufficient for in-orbit micro-vibration isolation.

To overcome the disadvantages associated with passive isolation, active isolation has been widely studied for nearly two decades. Active isolation is usually conducted by two different types of isolators: hard active isolators (HAIs) and soft active isolators (SAIs).

HAIs use a stiff actuator (either piezoelectric or Terfenol-D) in series with a spring. Refs.[12–16] investigated various vibration isolation assemblies for precision payloads that employed piezoelectric HAIs, and Refs.[17–19] studied isolation assemblies with Terfenol-D HAIs. The HAI assemblies have proved to be effective for narrowband isolation. For broadband isolation, the control force of an HAI must be applied over a wide range of frequencies, leading to complex control algorithms and requiring powerful acquisition/operation electronics, high power consumption, and precision sensors, which are inappropriate for space applications.

SAIs generally use a soft actuator, typically a voice coil motor, in parallel with a soft spring. Although SAIs require that the payload mass be off-loaded during ground testing and satellite launching, they have lower corner frequency than HAIs, so they allow much lower frequencies to be isolated and consume less on-board resources in broadband isolation. Refs.[20–23] discussed spacecraft hexapod isolators, which were composed of voice coil motor SAIs with suspended permanent magnets. The main disadvantage of this configuration is that the permanent magnet, which is located on the bottom flexible joint, decreases the local mode frequency of the SAI, while inducing excessive stress on the flexible joint. Refs.[24–28] showed a more appropriately designed hexapod isolator with voice coil motor SAIs, in which the permanent magnet was fixed. In this configuration, the permanent magnet is attached to the base, and the membrane performs the functions of both the axial spring and the bottom flexible joint. Refs.[29,30] demonstrated the concept of a disturbance-free payload architecture for active isolation as well as precision steering of a payload, which was controlled by non-contact voice coil motor SAIs. Ref.[31] fabricated several active vibration isolation assemblies for international space station micro-gravity experiments, which were controlled by the levitation of various electromagnetic SAIs. Although the isolation assemblies with non-contact or levitation SAIs exhibited good performance, the complexity of the system design and controls decreases their reliability and restricts applications on unmanned satellites.

Thus, previous work has shown that an SAI is more suitable for satellite vibration isolation in regard to isolation performance, technology maturity, and consumption of on-board resources. However, few studies have focused on the low-noise design of an SAI system for micro-vibration as well as SAI vibration isolation experimental verification with micro-vibration excitation. In this paper, a voice coil motor SAI with a fixed permanent magnet was studied. There were one active degree-of-freedom (DOF) along the axis of the SAI and five passive DOFs, making the SAI applicable to not only localised (single-axis) isolation but also systematic (multi-axis) isolation when forming an isolation mount (e.g., tripod, hexapod, or octopod).

In addition to the SAI system design and analysis, this paper reports on (1) the six DOFs stiffness calculation of the SAI membrane in large deformation, (2) the development of a low-noise linear driver for the SAI with a high-speed buffer, and (3) the SAI micro-vibration isolation experiments in frequency domain and time domain to verify the control effect and stability.

This paper begins with a discussion of the demands of satellite micro-vibration isolation and a summary of the isolation approaches that have been used or studied. Next, the design, analysis, and manufacture of the mechanical unit and the low-noise linear driver of a voice coil motor SAI are studied. Then, rigid-flexible coupling dynamic modelling of the SAI based on the Catia-Patran/Nastran-Adams software platform and an analysis of the SAI are conducted, and a sky-hook damper for active control is designed and simulated. Finally, experimental results of the SAI are shown, including driver noise, dynamic response, and frequency/time domain isolation.

2. Design and manufacture of SAI

2.1. Mechanical unit

Fig. 1 shows the schematic of the mechanical unit of the SAI. As shown in the figure, a permanent magnet, the heaviest part of the mechanical unit, is attached to the base. A single membrane performs the functions of both the spring for axial compliance and the U-joint. A rod is attached to the central point of the membrane, supports the coil on the left side and connects to the flexible joint on the right side, which in turn is connected to the payload as a ball joint. In this design, the rod axis is allowed to rotate with respect to the magnet at the central point of the membrane. This capability results in an increase in the magnetic gap of the voice coil motor, which slightly decreases the force sensitivity. The one active DOF on the SAI is the axial movement of the coil, and the five passive DOFs are the rotation and torsion of the membrane and the flexible joint. Figs. 2 and 3 show a cutaway view and a photo of the mechanical unit.

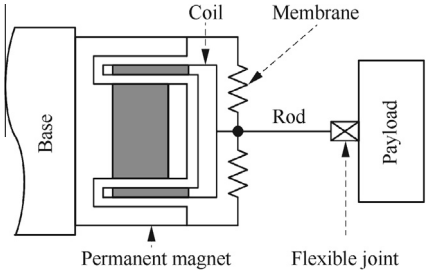

Fig. 1 Schematic of mechanical unit.

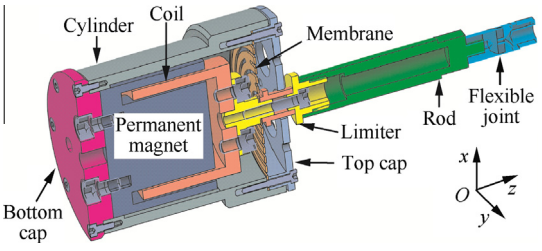

Fig. 2 Cutaway view of mechanical unit.

Fig. 3 Photo of mechanical unit.

(1) Voice coil motor

The voice coil motor used in this paper is a ferromagnetic core radial polarity toroid manufactured by Chenyang Auto Tech. The peak/continuous force is 80 N/21.8 N, the stroke is ±2.5 mm, the force sensitivity is 12.7 N/A, and the mass of the coil/magnet assembly is 45 g/215 g. The gap between the coil and the magnet allows the rod to rotate approximately 1°.

(2) Membrane

The membrane is a key component in the mechanical unit of the SAI. Its structural characteristics should satisfy the following criteria: (1) a lower axial stiffness to decrease the corner frequency of the SAI, (2) a minimum rotational stiffness to reduce additional torque, and (3) high lateral and torsional stiffness with and without membrane deformation to restrict the shear and twist of the coil.

In this paper, the membrane is made of a beryllium copper alloy and is designed to achieve a 1 Hz axial resonance frequency when the SAI is coupled to a 50 kg payload. The design stiffness is 1974 N/m. The major procedures associated with membrane design included adjusting the size, number, and distribution of chambered slits (Fig. 4) and assigning the diameters of the outer and inner circles according to the dimensions of the voice coil motor. To obtain precise values with the deformation, a non-linear finite element (FE) analysis was performed to determine the various degrees of stiffness of the designed membrane. The material properties used in the analysis were an elastic modulus of 127.5 GPa, a Poisson ratio of 0.3, and a density of 8.25 g/cm^3. The FE model is shown in Fig. 4.

In this paper, the membrane stiffness from the six DOFs is computed in the equilibrium position with and without elastic

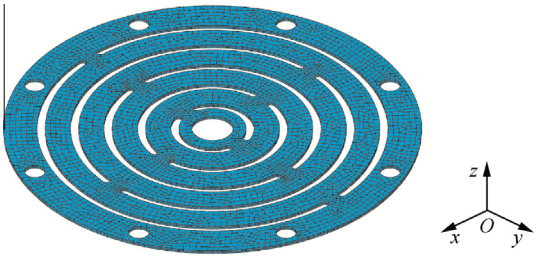

Fig. 4 Membrane FE model.

deformations. The stiffness is indirectly obtained by measuring the elongations along the x, y, and z axes versus the load as well as the deflections around the x, y, and z axes versus the torsion. Table 1 shows the computed membrane stiffness values. The values show that (1) compared with the design stiffness, the error of the computed axial stiffness (along z) in the equilibrium position is relatively small (4.86%); (2) compared with the equilibrium position, the variation in the axial stiffness, when extended and rotated, is relatively small (within 10%); (3) the rotational stiffness (around x and y) is low, and the variation in the rotational stiffness, when extended and rotated, is very small (within 1.5%); (4) the lateral stiffness (along x and y) is high, and the variation in the lateral stiffness, when rotated, is very small (within 1.5%), while the variation, when extended, is relatively large (28.29% and 61.25%, respectively); (5) the torsional stiffness (around z) is high, and the variation in the torsional stiffness, when extended and rotated, is relatively small (within 5%).

The membrane is manufactured with a thickness of 0.3 mm, using a standard chemical etching process to minimise machining induced stress and deformation. Then, a three-hour heat preservation aging treatment inside a vacuum return air furnace was performed. Fig. 5 shows the photo of the membrane.

(3) Flexible joint

The flexible joint should approximate a ball joint to connect to the payload, to ensure that the maximum axial stiffness and minimum rotational/torsional stiffness are maintained. Although many kinds of flexible joint designs have been studied, this paper adopts a typical form as studied in Ref.[32] (see Fig. 6). In order to achieve a high yield strength and a low elastic modulus, titanium was selected as the joint material. A non-linear FE analysis was performed to determine the various degrees of stiffness of the flexible joint used in the membrane design. The material properties used in the analysis were an elastic modulus of 106.4 GPa, a Poisson ratio of 0.3, and a density of 4.51 g/cm^3. The FE model is shown in Fig. 6. Because of the stiffness serial characteristics of the flexible joint and the membrane, as well as the much lower

Table 1 Membrane computed stiffness.

Deformation case	Stiffness along axial direction (N/m)			Stiffness around axial direction (N·m/rad)		
	Along x	Along y	Along z	Around x	Around y	Around z
Equilibrium position without deformation	8.185×10^5	9.486×10^5	2.070×10^3	0.2287	0.2632	86.4135
1 mm axial elongation	5.870×10^5	3.679×10^5	2.275×10^3	0.2321	0.2657	82.3856
1° rotation about x	8.181×10^5	9.351×10^5	2.069×10^3	0.2287	0.2632	83.2794
1° rotation about y	7.966×10^5	9.476×10^5	2.068×10^3	0.2287	0.2632	83.1591

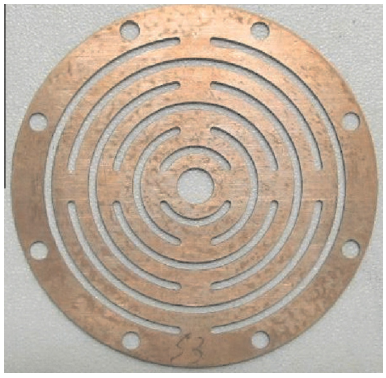

Fig. 5 Photo of membrane.

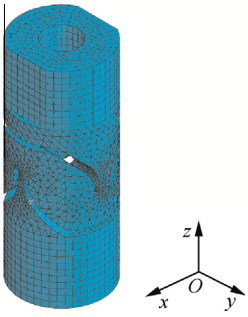

Fig. 6 Flexible joint FE model.

stiffness of the membrane, the deformations of the flexible joint are very small. The stiffness values from the six DOFs of the flexible joint in the equilibrium position without elastic deformation are computed and listed in Table 2.

The flexible joint was manufactured by electro-erosion, with a photo shown in Fig. 7.

(4) Other parts

Other parts of the SAI include top/bottom caps, a cylinder, a rod, limiters, and so on. All of these parts are made of aluminium and shown in Fig. 2.

2.2. Low-noise driver

The disturbance levels for micro-vibration are always low. To achieve isolation, the electrical noise from the SAI driver should be highly restricted. The existing driver in our laboratory is a pulse-width modulation (PWM) power amplifier, with power delivered by a Mosfet H-bridge stage. Because a ripple current is inevitably produced by the PWM chopper, the electrical noise of the PWM power amplifier is relatively high.

Fig. 7 Photo of flexible joint.

In this paper, to replace the PWM one, a low-noise linear driver with a high-speed buffer was designed, built, and tested for performance.

Fig. 8 shows the schematic circuit diagram of the driver. A_1 and A_2 are operational amplifiers (model OP07). A_1 and R_1–R_3 compose a follower to decrease the influence of the load voltage on the input voltage (namely, $U_I = u_i$). As an induced current will be produced when a coil moves in a magnetic field, the driver should experience current negative feedback to preserve the ratio between the input voltage (U_I) and the output current (I_O). A_2, P, and R_4–R_6 compose a "voltage-current" converter to provide current negative feedback. R_L is the load (coil). P is a high-speed buffer (model BUF634) and is used as a current amplifier. The BUF634 high-speed buffer operates on 1.5 mA quiescent current with maximum 250 mA output, 2000 V/ms slew rate, and a 30 MHz bandwidth. Because the BUF634 is an operational amplifier chip, its electrical noise is much lower than that of the power amplifier chip. Its output current is relatively low but is suitable for the micro-vibration conditions, where the power consumption is low. Furthermore, the BUF634 can be connected in parallel to multiply the output current if needed.

Fig. 9 shows a photo of the low-noise driver, in which eight BUF634 high-speed buffers are used, and the maximum output is 1 A (another 1 A is shunted by the feedback resistors). The testing of the driver is described in Section 5.2.

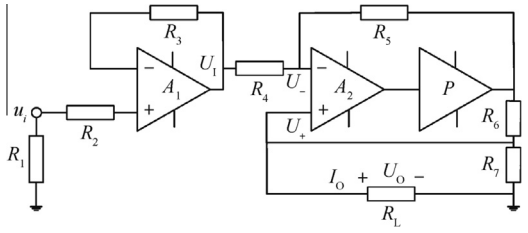

Fig. 8 Schematic circuit diagram of driver.

Table 2 Flexible joint computed stiffness.

Deformation case	Stiffness along axial direction (N/m)			Stiffness around axial direction (N·m/rad)		
	Along x	Along y	Along z	Around x	Around y	Around z
Equilibrium position without deformation	2.9531×10^6	3.0294×10^6	1.3817×10^7	2.8517	2.8455	27.8735

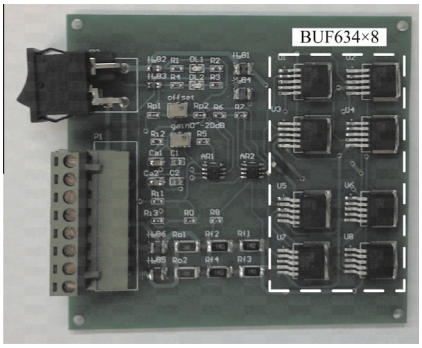

Fig. 9 Photo of driver.

3. Dynamic modelling and analysis of SAI

3.1. Dynamic modelling

The SAI is composed of both rigid (magnet, coil, etc.) and flexible (membrane and flexible joint) parts, so a rigid-flexible coupling dynamic model of the SAI was built with the Catia-Patran/Nastran-Adams software platform.

Firstly, CAD models of the SAI parts were built with Catia, so that dimensions, masses, and inertia properties could be established. For the rigid parts, the CAD models were converted into .CMD files by Catia/SimDesigner and imported into Adams. For the flexible parts, the CAD models were imported into Patran/Nastran and analysed after carrying out operations necessary to run the models: assigning the material properties, defining the element properties, meshing, and creating multi-point constraints (MPCs). The membrane was meshed with Hexahedron elements, and the flexible joint was meshed with Tetrahedron elements Tet10. The MPC points were used as constraint points for the forces in Adams, thereby establishing the connections between the flexible and rigid parts. Eight points on the membrane's outer circle were defined as MPC points, as well as the central point of the inner circle. Meanwhile, 2 ends of the flexible joints were defined as MPCs. The Nastran analysis was then conducted, and a modal neutral file (.MNF) was created, including the model geometry, nodal mass and inertia, mode shapes, and so on. Finally, the .MNF files were imported into Adams.

In this way, the rigid and flexible parts were assembled in Adams, and the rigid-flexible coupling dynamic model of the SAI was created.

3.2. Analysis

Mode and frequency analysis of the SAI was conducted. The former six mode shapes and frequencies are listed in Table 3. Modes 1–3 and 4–6 are mainly the deformations of the membrane and the flexible joints, respectively. The six responsive modes in the frequency band of 0.084–2.240 Hz show the appropriateness of the designs of the membrane and the flexible joints.

In the frequency analysis, a sinusoidal signal varying from 0.01 to 1.00 kHz was applied to the bottom of the SAI along the z axis. In order to interpret the results and assess the performance of the design, the mean-square-root (MSR) value of the responses on the payload along x, y, and z axes was calculated.

Table 3 Computed mode shapes and frequencies of SAI.

Mode	Mode shape	Frequency (Hz)
1	Tilting around x of membrane	0.084
2	Tilting around y of membrane	0.085
3	Piston along z of membrane	1.076
4	Tilting around x of flexible joint	1.605
5	Tilting around y of flexible joint	1.621
6	Twisting around z of flexible joint	2.240

4. Controller design

The simplified dynamic model of the SAI is shown in Fig. 10. The variables M, k, and c are mass, stiffness, and damping, and the variables F_a, x_b, and x_p are the control force, the base displacement, and the payload displacement. When $F_a = 0$, the SAI is a passive isolated system, and the transmissibility is defined as

$$\frac{x_p(s)}{x_b(s)} = \frac{cs+k}{Ms^2+cs+k} = \frac{1+2\xi s/\omega_n}{1+2\xi s/\omega_n+(s/\omega_n)^2} \tag{1}$$

where the natural frequency $\omega_n = \sqrt{k/M}$ and the damping ratio $\xi = c/2\omega_n M$.

Fig. 11 shows the transmissibility curves for different values of ξ. When the angular frequency $\omega < \sqrt{2}\omega_n$, increasing ξ will reduce the transmissibility amplitude, particularly at the resonance frequency. However, when $\omega > \sqrt{2}\omega_n$, increasing ξ will

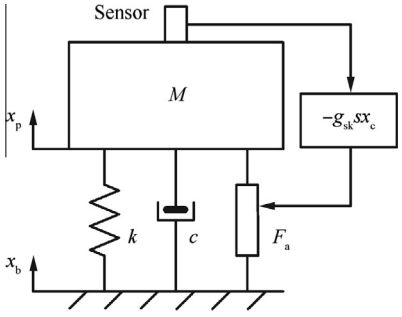

Fig. 10 Simplified dynamic mode of SAI.

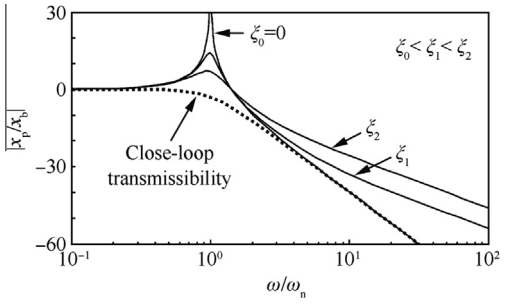

Fig. 11 Transmissibility of SAI.

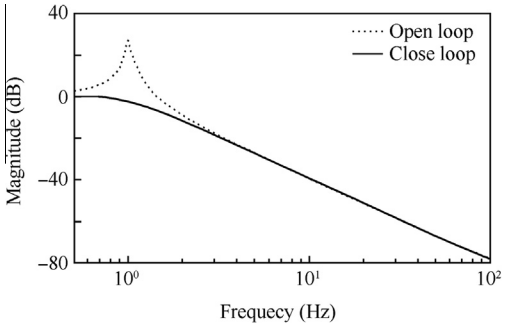

Fig. 12 Numerical simulation of transmissibility.

increase the transmissibility amplitude and the asymptotic decay rate, which deteriorates from −40 dB/dec to −20 dB/dec.

In order to solve this conflict, a simple feedback control strategy, a skyhook damper,[33] is introduced, for which the control force, $F_a(s) = -g_{sk}sx_d$, where g_{sk} is the control gain, is proportional to the absolute velocity of the payload. Then, the closed-loop transmissibility of the isolator is defined as

$$\frac{x_p(s)}{x_b(s)} = \frac{cs+k}{Ms^2+(g_{sk}+c)s+k} \tag{2}$$

When $c << g_{sk}$ and $c \approx 0$, the system is approximated by a second-order oscillation cell:

$$\frac{x_p(s)}{x_b(s)} = \frac{k}{Ms^2+g_{sk}s+k} = \frac{1}{1+2\bar{\xi}s/\omega_n+(s/\omega_n)^2} \tag{3}$$

where the damping ratio $\bar{\xi} = g_{sk}/2\omega_n M$. The closed-loop transmissibility curve is shown as the dotted line in Fig. 11. The asymptotic curve at low frequency is a 0 dB line, while at high frequency, the asymptotic curve is a −40 dB/dec line, which crosses the 0 dB line at ω_n. When $\bar{\xi}$ is larger than the critical damping ratio of $1/\sqrt{2}$, the resonance peak is removed.

By using the model shown in Fig. 10, the transmissibility of the SAI was numerically simulated. According to the actual system, a controller was designed, and the SAI parameters were $M = 50.137$ kg, $k = 2061$ N/m, $c = 21$ N/(m·s^{-2}) (experimentally determined), and $g_{sk} = 455$ (when $\bar{\xi}$ is the critical damping ratio). The result (Fig. 12) shows the effects from the controller.

5. Experiment

5.1. Experimental setup

Fig. 13 shows the experimental setup for the SAI. To eliminate the effects of gravity, the mechanical unit of the SAI, a 50 kg payload, and an electromagnetic exciter were horizontally suspended, with the exciter fixed to the base. To protect the payload from any micro-vibrations, even slight friction within the mechanical unit of the SAI must be avoided. Therefore, the three parts are finely aligned to ensure that they remain coaxial.

A high-precision single-axis accelerometer (LANCE Tech. Inc., model: LC0116) and a medium-precision 3-axis accelerometer (LANCE Tech. Inc., model: LC0111) were fixed on the payload for closed-loop control and response measurement, respectively. Another LC0116 accelerometer was fixed on the exciter used for micro-vibration generation.

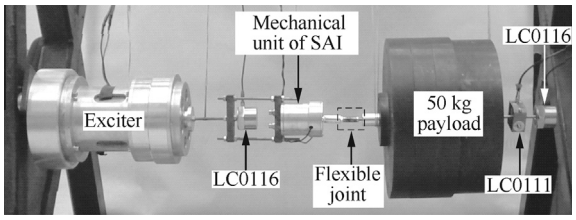

Fig. 13 Experimental setup used in testing SAI.

5.2. Results

(1) Noise testing

To evaluate the electrical noise from the low-noise driver, the noise from the payload when the driver powered on/off for a 0 V input situation was examined. Fig. 14 shows the payload noise acquired by the model LC0116 accelerometer. When powered on, the payload acceleration induced by the electrical noise from the low-noise driver was identical to the background noise when the driver was powered off. Furthermore, the payload noise derived from the laboratory's existing driver (Everbloom Sys., model: 4122Z) was also examined (dotted line in Fig. 14), and the acceleration induced from the electrical noise of this driver was found to be much higher.

(2) Frequency analysis

A $10 \times 10^{-3}g$ sweep excitation was applied on the bottom of the SAI along the z axis, similar to the simulation described in

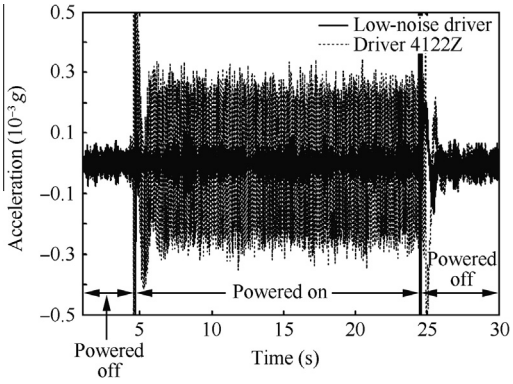

Fig. 14 Payload noise.

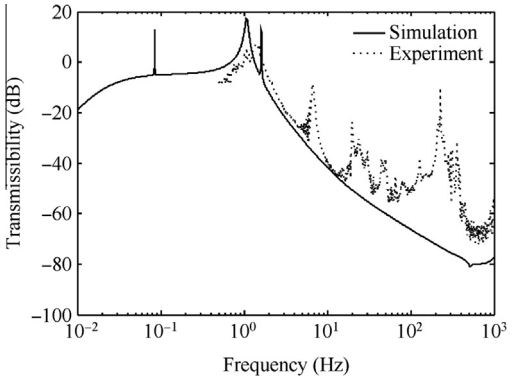

Fig. 15 MSR value of payload response.

Section 3.2. Because of the performance limitations of the electromagnetic exciter, the minimum frequency in this experiment was higher than that in the simulation. The frequency range examined was 0.5–1000 Hz. The MSR value of the three output channels of the LC0111 accelerometer (responses along the x, y, and z axes) is shown as the dotted line in Fig. 15. The consistency of asymptotic decay rate between the experimental and simulated transmissibility is good. Because of certain dynamic model errors, such as the deviation of the membrane stiffness and the damping coefficient, the frequency errors of mode frequency in the simulated values can be found in Fig. 15. Furthermore, the nonlinear effects, such as mode frequency of suspending truss and additional parts, are ignored in the dynamic model, so the high mode frequency cannot exhibit in the simulated values.

(3) Isolation effects in the frequency domain

A $2\times10^{-3}g$, 0.5–100 Hz sweep excitation was applied on the bottom of the SAI along the z axis, with a control gain of g_{sk} = 455. Fig. 16 shows the experimental transmissibility and the phase delay with and without using control. The result shows that the resonance peak is significantly suppressed, the attenuations are more than −10 dB and −20 dB above 2.4 Hz and 5 Hz, respectively, and the mean value of the absolute acceleration in the 5–100 Hz range is $0.156\times10^{-3}g$.

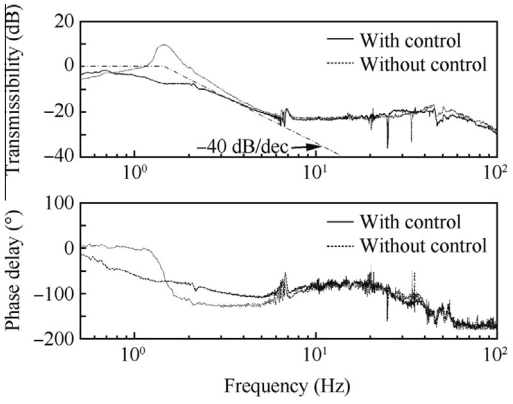

Fig. 16 Experimental transmissibility with and without control.

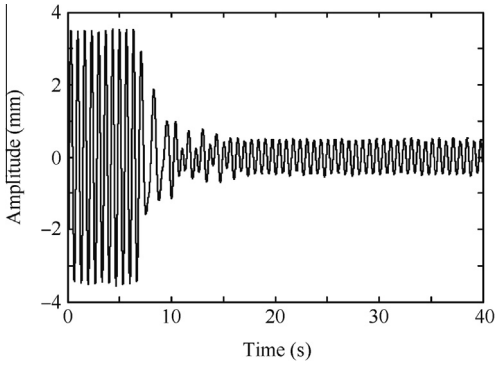

Fig. 17 Experimental amplitude at resonance frequency with and without control.

(4) Isolation effects in the time domain

A study in the stability of the control system, examining the effects of isolation in the time domain, was also conducted. A $0.5\times10^{-3}g$, 1.43 Hz (the actual resonance frequency along the z axis) sinusoidal excitation was applied on the bottom of the SAI, with a control gain of g_{sk} = 455. Fig. 17 shows the experimental amplitude with and without using control. The results show that the amplitude significantly decreases after the control takes effect, approximately 7 s, and the effect is stable.

6. Conclusions

An SAI has been designed and tested for use in satellite micro-vibration isolation. The mechanical unit of the SAI consists of a voice coil motor, a membrane, and a flexible joint, and the low-noise driver for the SAI is current-amplified by a high-speed buffer. A rigid-flexible coupling dynamic model of the SAI was built and analysed, and a sky-hook damper was designed for use as a control. The experimental results show that:

(1) The SAI's payload acceleration induced by the electrical noise from the low-noise driver is similar to that from the background noise.
(2) The experimental and simulated transmissibility from the frequency analysis agree well.
(3) With the sky-hook damper, the resonance peak is significantly suppressed, attenuations are more than −20 dB above 5 Hz, and the control effect is stable. Furthermore, the experimental isolation transmissibility is consistent with those of other SAIs,[34] which shows the effectiveness of the designed SAI and the controller.

Acknowledgements

The authors would like to thank the anonymous reviewers for their critical and constructive review of the manuscript. The study was co-supported by the National Natural Science Foundation of China (No. 11302010) and Shanghai Institute of Satellite Engineering (No. HT-2010-0753).

References

1. Wittig M, Holtz LV, Tunbridge DEL. In-orbit measurements of microaccelerations of ESA's communication satellite OLYMPUS. *Proceedings of free-space laser communication technologies II*; 1990 Jan 14; Los Angeles (CA). Washington, D.C.: SPIE; 1990. p. 205–14.
2. Arnon S, Kopeika NS. Laser satellite communication network-vibration effect and possible solutions. *Proc IEEE* 1997;**85**(10):1646–61.
3. Orszulik RR, Shan JJ. Active vibration control using genetic algorithm-based system identification and positive position feedback. *Smart Mater Struct* 2012;**21**:1–10.
4. Oh HU. Performance investigation of spaceborne micro-vibration isolation system combined with heat pipe cooling system. *64th international astronautical congress*; 2013. p. IAC-13-C2-1-11.
5. Edeson R, Aglietti GS, Tatnall ARL. Conventional stable structures for space optics: the state of the art. *Acta Astronaut* 2010;**66**(1–2):13–32.

6. Agrawal B, Jitter control for imaging spacecraft. *4th international conference on recent advances in space technologies*; 2009 June 11–13; Istanbul, Turkey. New York: IEEE; 2009. p. 615–20.
7. Bronowicki AJ. Vibration isolator for large space telescopes. *J Spacecraft Rockets* 2006;**43**(1):45–53.
8. Miller SD, Swensony ED, Cobb RG. Investigation of a novel compact vibration isolation system for space applications. Reston: AIAA; 2010. Report No.: AIAA-2010-2935.
9. Camelo V, Simonian S, Brennan S. Viscoelastic damping of structural joints for disturbance isolation and vibration attenuation. Reston: AIAA; 2009. Report No.: AIAA-2009-2522.
10. Davis P, Cunningham D, Harrell J. Advanced 1.5 Hz passive viscous isolation system. Reston: AIAA; 1994. Report No.: AIAA-1994-1651-CP.
11. Marneffe B, Avraam M, Deraemaeker A. Vibration isolation of precision payloads a six-axis electromagnetic relaxation isolator. *J Guidance Control Dyn* 2009;**32**(2):395–401.
12. Hyand DC, King JA, Davis LD. Active vibration isolation with stiff actuators and inertial sensors. *Proceedings of actuator technology and applications*; 1996 Aug 4; Denvor (CO). Washington, D.C.: SPIE; 1996. p. 93–101.
13. Claster RJ, Garba JA. STRV-1B cryocooler vibration suppression. Reston: AIAA; 1995. Report No.: AIAA-1995-1122-CP.
14. Defendini A, Vaillon L, Trouve F. Technology predevelopment for active control of vibration & very high accuracy pointing systems. *ESA's 4th spacecraft guidance, navigation and control systems conference*; 1999. p. 1–7.
15. Anderson EH, Fumo JP, Erwin RS. Satellite ultraquiet isolation technology experiment (SUITE). *IEEE Aerospace Conference*; 2000.
16. McMickell MB, Kreider T, Hansen E. Optical payload isolation using the miniature vibration isolation system (MVIS-II). *Proceedings of industrial and commercial applications of smart structures technologies*; 2007 Mar 18; San Diego, USA. Washington, D.C.: SPIE; 2007. p. 1–7.
17. Haynes L, Geng Z, Teter J. A new terfenol-D actuator design with applications to multiple DOF active vibration control. *Proceedings of smart structures and materials/smart structures and intelligent systems*; 1993 Feb 1; Albuquerque (NM). Washington, D.C.: SPIE; 1993. 1917: p. 919–28.
18. Nakamura Y, Nakayama M, Masuda K. Development of a uniaxial hybrid actuator using the combination of an air actuator and a giant-magnetostrictive actuator. *Smart Mater Struct* 2002;**11**:361–9.
19. Li C, Mao JJ. Active vibration control under the actuator with magnetic hysteresis loop. *International conference on control and automation*; 2005 Jun 26–29; Budapest, Hungary. New York: IEEE; 2005. p. 914–8.
20. Spanos J, Rahman Z, Blackwood G. A soft 6-axis active vibration isolator. *Proceedings of the American control conference*; Seattle (WA); 1995.
21. McInroy JE, Hamann JC. Design and control of flexure jointed hexapods. *IEEE Trans Robotics Automation* 2000;**16**(4), 372-1.
22. Taranti CGR, Agrawal BN, Cristi R. An efficient algorithm for vibration suppression to meet pointing requirements of optical payloads. Reston: AIAA; 2001. Report No.: AIAA-2001-4094.
23. Hanieh AA, Horodinca M, Preumont A. Stiff and soft stewart platforms for active damping and active isolation of vibrations. *8th international conference on new actuators*; Bremen; 2002.
24. Cobb RG, Sullivan JM, Das A. Vibration isolation and suppression system for precision payloads in space. *Smart Mater Struct* 1999;**8**:798–812.
25. Thayer D, Campbell M, Vagners J. Six-axis vibration isolation system using soft actuators and multiple sensors. *J Spacecraft Rockets* 2002;**39**(2):206–12.
26. Brennn SM, Bronowicki AJ, Ryan PJ. Control structure interaction testbed: passive isolation, simulation & test. Reston: AIAA; 2006. Report No.: AIAA-2006-1834.
27. Preumonta A, Horodincaa M, Romanescu I. A six-axis single-stage active vibration isolator based on Stewart platform. *J Sound Vib* 2007;**300**:644–61.
28. Sannibale V, Ortiz GG, Farr WH. A sub-hertz vibration isolation platform for a deep space optical communication transceiver. *Proceedings of free-space laser communication technologies XXI*; 2009 Jan 24; San Jose (CA). Washington, D.C.: SPIE; 2009. p. 1–9.
29. Pedreiro N, Carrier AC, Lorell KR. disturbance-free payload concept demonstration. Reston: AIAA; 2002. Report No.: AIAA-2002-5027.
30. Dewella L, Pedreiroa N, Blaurockb C. Precision telescope pointing and spacecraft vibration isolation for the terrestrial planet finder coronagraph. *Proc SPIE* 2005;**5899**:1–14.
31. Grodsinsky CM, Whorton MS. Survey of active vibration isolation systems for microgravity applications. *J Spacecraft Rockets* 2000;**37**(5):586–96.
32. Anderson EH, Cash MF, Hall JL. Hexapods for precision motion and vibration control. *Proceedings of control of precision systems*; 2004 April. Raleigh (NC): ASPE. 2004. p. 1–5.
33. Kaplow CE, Velman JR. Active local vibration isolation applied to a flexible space telescope. *J Guidance Control* 1980;**3**(3):227–33.
34. Hanieh AA. Active isolation and damping of vibrations via stewart platform [dissertation]. Bruxelles: Universite Libre de Bruxelles; 2003.

Li Weipeng received his B.S. degree in computer science and technology from Northwest Polytechnical University in 2002 and his Ph.D. degree in spacecraft design from Beihang University in 2008. His main research interests are spacecraft vibration isolation and flexible structure vibration suppression.

Huang Hai received his B.S., M.S., and Ph.D. degrees in aerospace engineering in 1983, 1986, and 1990, respectively, all from Beihang University (BUAA). He is now a professor, vice dean of the school, as well as the department chair. His interested research areas include concept design of spacecraft, structural and multi-disciplinary optimization, adaptive/smart structures & mechanisms and control, and the related applications in aerospace engineering.